

# Visible Light Active Silver Decorated Iron Titanate/Titanium Dioxide Nanohybrid for Sterilization of Explants Grown by In Vitro Technique

Kasun L. Seneviratne, Imalka Munaweera, Sriyani E. Peiris,\* Piyumi Kodithuwakku, Colin N. Peiris, and Nilwala Kottegoda\*

Visible light (VL) active silver decorated iron titanate/titanium dioxide (Ag-FeTiO<sub>3</sub>/TiO<sub>2</sub>) nanohybrids derived from natural ilmenite sand effectively cleanse the exophytic plant pathogens in explants grown by in vitro techniques. VL active nanohybrid is synthesized by acid-hydrolysis of natural ilmenite, followed by precipitation of the lixivium and decoration with Ag onto FeTiO<sub>3</sub>/TiO<sub>2</sub> nanoparticles, and finally calcination under a nitrogen environment to obtain Ag-FeTiO<sub>3</sub>/TiO<sub>2</sub>. A morphological study conducted using transmission electron microscopy (TEM) confirms the formation of Ag-FeTiO<sub>3</sub>/TiO<sub>2</sub>. Powder X-ray diffraction (PXRD) analysis shows that the nanohybrid primarily consists of anatase, iron titanate (FeTiO<sub>3</sub>), Ag<sub>2</sub>O, and Ag. X-ray photoelectron spectroscopy (XPS) study suggests the presence of Ag<sup>0</sup>/Ag<sub>2</sub>O/Fe<sub>2</sub>O<sub>3</sub> composites on the FeTiO<sub>3</sub>/TiO<sub>2</sub> particle surface. The optical band gap significantly changes from 3.14 eV (ilmenite) to 2.80 eV after the decoration of FeTiO<sub>3</sub>/TiO<sub>2</sub> with Ag. This nanohybrid is utilized as a surface-sterilizing agent for in vitro establishment of the *Dracaena sanderiana* Sander ex Mast plant. Findings illustrate Ag-FeTiO<sub>3</sub>/TiO<sub>2</sub> nanohybrid-based photo-sterilization leads to the survival of 90% of the microbes' free cultures while the material can be re-used due to its photocatalytic behavior. Thus, the newly synthesized nanohybrid can replace harmful sterilization agents used in tissue culture techniques.

## 1. Introduction

Micropropagation, the plant in vitro culture, is the commonly used technique to produce large quantities of uniform, true-to-type plants to meet the demand of commercial plant production.<sup>[1]</sup> The micro-propagated plants are healthy, vigorous, and available at any season of the year. All plant species introduced to micro-propagation are from the septic in vivo environment.<sup>[2]</sup> This becomes the major drawback as the elimination of micro-organisms<sup>[3]</sup> should be undertaken with uttermost care not to damage the delicate plant parts known as explants which are introduced to establish in vitro cultures.<sup>[4]</sup> Hence, to prevent microbial infections, surface sterilization is applied as the first step of explant introduction to the micro-propagation process.<sup>[5]</sup> Previous reports state chemical sterilization is the most commonly used technique due to its high efficacy and reduced cost than physical sterilization techniques.<sup>[4]</sup> Mercuric chloride (HgCl<sub>2</sub>), sodium hypochlorite (NaOCl), alcohol, benzalkonium chloride,


and peroxide (H<sub>2</sub>O<sub>2</sub>) are widely used chemicals as disinfecting agents<sup>[1,4,6]</sup> for explant establishment in vitro. However, some of these chemicals are carcinogenic and the toxicity of the chemicals has adverse effects on the environment, and human health.<sup>[7]</sup> An alternative technique, to replace such toxic chemicals, which is highly efficient, low-cost, and reusable would lead to major breakthroughs in the tissue culture industry.

In modern scientific research, photocatalytic sterilization of various surfaces including, hospitals, textiles, and packaging has received high attention since the method is more environmentally friendly and efficient. Reactive oxygen species (ROS) are the most effective chemical species which can be utilized in such applications.<sup>[8,9]</sup> ROS radicals directly damage microbial cell membranes and internal organelles such as mitochondria and nucleic acids.<sup>[9]</sup> Thus, the ROS sterilization technique using photocatalytic materials becomes a more reliable route to sterilize plant tissues although it has not been studied thoroughly. Photocatalysts generate ROS radicals rapidly, abundantly, and continuously by absorbing photons.<sup>[10]</sup> Thus, photo-sterilization

K. L. Seneviratne, S. E. Peiris, C. N. Peiris  
Faculty of Humanities and Sciences  
Sri Lanka Institute of Information Technology (SLIIT)  
New Kandy Road, Malabe 10115, Sri Lanka  
E-mail: sriyani.p@sliit.lk

I. Munaweera, P. Kodithuwakku, N. Kottegoda  
Department of Chemistry  
Faculty of Applied Science  
University of Sri Jayewardenepura  
Gangodawila, Nugegoda 10250, Sri Lanka  
E-mail: nilwala@sjp.ac.lk

I. Munaweera  
Instrument Center  
Faculty of Applied Sciences  
University of Sri Jayewardenepura  
Gangodawila, Nugegoda 10250, Sri Lanka

 The ORCID identification number(s) for the author(s) of this article can be found under <https://doi.org/10.1002/admt.202201292>.

DOI: 10.1002/admt.202201292

**Table 1.** Chemical composition of ilmenite based on X-ray fluorescence spectroscopy (XRF) analysis.

Oxide	TiO <sub>2</sub>	Fe <sub>2</sub> O <sub>3</sub>	SiO <sub>2</sub>	Al <sub>2</sub> O <sub>3</sub>	Cr <sub>2</sub> O <sub>3</sub>	MnO	MgO	ZrO <sub>2</sub>	P <sub>2</sub> O <sub>5</sub>	CaO	Cl
W.t. %	57.52	29.75	5.23	1.10	0.12	0.67	1.15	0.25	0.12	0.04	4.05

has future potential as an inexpensive, eco-friendly, reusable, and simple technique to be used in the tissue culture industry. Many photocatalytic materials have been tested for in vitro culture applications.<sup>[11]</sup> For example, nano TiO<sub>2</sub> is a well-known photocatalyst used due to its unique characteristics such as highly efficient photocatalytic action, inertness, low cost, and user-friendliness.<sup>[12]</sup> However, due to the wide band gap (BG) of TiO<sub>2</sub>, the high rate of electron-hole pair recombination and the need for UV region energy have limited its practical applications.<sup>[13]</sup> Therefore, many attempts have been made to reduce the band gap of TiO<sub>2</sub> using various structural modifications.<sup>[14,15]</sup> Recent studies showed that Fe-doped TiO<sub>2</sub> nanomaterials show intense photocatalytic activity under visible light compared to pristine TiO<sub>2</sub>.<sup>[13,16]</sup> Noble metal oxide like Ag<sub>2</sub>O has also been used as an efficient electron-capturing species, which prevents electron-hole pair recombination and hence, increases the rate of ROS generation.<sup>[17,18]</sup> Also, the plasmonic effect of noble metals such as metallic silver (Ag<sup>0</sup>) helps to reduce the band gap of TiO<sub>2</sub>.<sup>[19]</sup> In addition, a synergetic effect arising from the disinfectant properties of Ag and Fe and the presence of nanoparticles which leads to an increased aspect ratio further enhances the antimicrobial properties of hybrid materials.<sup>[20]</sup> Thus, the co-existence of Ag<sup>0</sup>/Ag<sub>2</sub>O/Fe<sub>2</sub>O<sub>3</sub> oxides with TiO<sub>2</sub> enhances antimicrobial properties more than pristine TiO<sub>2</sub>.<sup>[21]</sup> Traditionally, FeTiO<sub>3</sub> used in catalysis applications has been synthesized from TiO<sub>2</sub> which is extracted from natural minerals and few attempts have been made to use the modified naturally occurring ilmenite as a visible light active photocatalytic material.<sup>[22–26]</sup>

The present study describes a method to synthesize Ag decorated FeTiO<sub>3</sub>/TiO<sub>2</sub> nanohybrid derived from natural ilmenite as the precursor material and its application in photo-sterilization of plant tissues (plant nodes). Ag-FeTiO<sub>3</sub>/TiO<sub>2</sub> nanohybrid was derived from Sri Lankan ilmenite (beach sand) and utilized in the VL region to eliminate plant exophytic pathogens.<sup>[27]</sup> Herein, we used commercially grown *Dracaena sanderiana* Sander (“White”) ex Mast. as the explant for the tissue culture experiment.

## 2. Experimental Section

### 2.1. Materials and Chemicals

Chemicals utilized in the study included HCl (Analytical Grade, 37% w/w), NaOH pellets (ACS Grade), and AgNO<sub>3</sub> (Analytical Grade, 99.5% pure) from Sigma-Aldrich, HNO<sub>3</sub> (Analytical Reagent, 69% w/w) from Himedia laboratories and deionized water (DI) was utilized during the experiment. TiO<sub>2</sub> nano-powder (Analytical Grade, 99.9% pure) and potato dextrose agar (PDA) were purchased from Sigma-Aldrich. Natural ilmenite (FeTiO<sub>3</sub>) was obtained from the Pulmoddai deposit on Sri Lanka’s east coast, distributed by Lanka Mineral Sands Ltd, Sri Lanka, and

used as received. The majority (82.5%) of the particles demonstrated a size range from 90 to 150 μm and the elemental composition is summarized in **Table 1**. The plant materials were collected from the dracaena mother plants grown in a protected house and *Fusarium oxysporum* standard cultures were obtained from the Department of Agriculture Sri Lanka.

### 2.2. Acid Leaching of Ilmenite

Acid leaching was conducted in a microwave digester (ETHOS EASY advanced, Milestone, Italy), with a maximum power of 1800 W and vessel model number MAXI-44, to extract Ti and Fe as indicated in the previous reports.<sup>[28]</sup> Ilmenite (30 g) was ground to a particle size of about 10 μm (Figure S1, Supporting Information). The resulting ilmenite (5 g) was mixed with 100–150 mL of conc. HCl and exposed to microwave irradiation (250–300 W power and 90 bar pressure) at 110 °C for 1 h.<sup>[28,29]</sup> The temperature (110 °C) was kept constant throughout the digestion period. This procedure was repeated three times to obtain the maximum dissolved ilmenite. The resulting solution was collected in a 1 L borosilicate container and kept at room temperature.

### 2.3. Synthesis of Ag-Decorated FeTiO<sub>3</sub>/TiO<sub>2</sub> Nanohybrid

The concentrated acid leachate solution contains TiO<sup>2+</sup>, Fe<sup>2+</sup>, and Fe<sup>3+</sup> ions.<sup>[30,31]</sup> Initially, 50 mL of DI water was mixed with 100 mL of the above solution and the resulting solution was neutralized by adding 5 M NaOH solution dropwise (0.5 mL min<sup>-1</sup>) under vigorous stirring at 600 rpm and heating at 280 °C. When the pH reached 7–8, brown-colored fine particles precipitated.<sup>[22]</sup> The mixture was further stirred for another 2 h. Next, the transparent top layer was removed by centrifuging. The residual layer was washed using 100 mL of dilute 0.1 M HNO<sub>3</sub> and 400 mL of DI water and stirred for 1–2 h with boiling to remove the Cl<sup>-</sup> ions.<sup>[32]</sup> This procedure was repeated to remove the maximum amount of Cl<sup>-</sup> ions from the residue. The removal of Cl<sup>-</sup> was verified by adding 2% silver nitrate (AgNO<sub>3</sub>) to the discarded water. The absence of white color cloudiness with 2% AgNO<sub>3</sub> that the residue was approximately free from Cl<sup>-</sup> ions.

Silver solution (250 mg L<sup>-1</sup>) was utilized for decorating FeTiO<sub>3</sub>/TiO<sub>2</sub> (prepared by dissolving 25 mg of AgNO<sub>3</sub> in 100 mL DI water). From the 250 mg L<sup>-1</sup> silver solution, a 40.00 mL portion was mixed with the 50.00 mL of residue solution to prepare the Ag-FeTiO<sub>3</sub>/TiO<sub>2</sub> nanohybrid. Further, FeTiO<sub>3</sub>/TiO<sub>2</sub> was synthesized using the same procedure but without adding Ag to the FeTiO<sub>3</sub> residue.

The resulting mixtures were ultrasonicated for 30 min (GT Sonic-3L, 45 kHz, 30 °C, 100 W ultrasonic power) in an aqueous medium. The sonicated mixtures were dried in a hot air oven

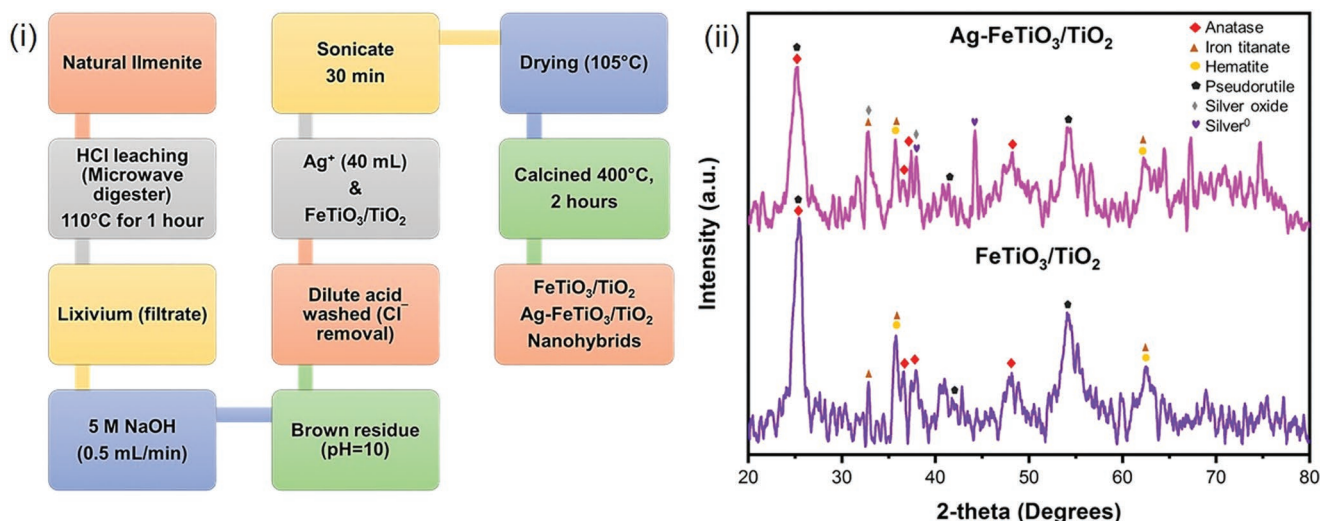


**Figure 1.** i) Schematic diagram of Ag-FeTiO<sub>3</sub>/TiO<sub>2</sub> and FeTiO<sub>3</sub>/TiO<sub>2</sub> synthesis method and ii) PXRD patterns of Ag-FeTiO<sub>3</sub>/TiO<sub>2</sub> and FeTiO<sub>3</sub>/TiO<sub>2</sub> nanohybrids.

(105 °C) for 6–8 h to evaporate water. The obtained dried residue was ground to a fine powder with a mortar and pestle. The resulting powder samples were calcined at 400 °C for 2 h in an inert atmosphere (N<sub>2</sub>) in order to obtain the Ag-FeTiO<sub>3</sub>/TiO<sub>2</sub> nanohybrid (see Figure 1a). The control sample of FeTiO<sub>3</sub>/TiO<sub>2</sub> was prepared in the same way without Ag.

#### 2.4. Characterization of FeTiO<sub>3</sub>/TiO<sub>2</sub> and Ag-FeTiO<sub>3</sub>/TiO<sub>2</sub> Nanohybrids

Powder X-ray diffraction (PXRD) studies were carried out using Rigaku Ultima-IV diffractometer with Cu K $\alpha$  radiation ( $\lambda = 1.5405 \text{ \AA}$ , 30 mA, 40 kV) to determine the structural characteristics of nanohybrids. The diffraction results were collected within a 2-theta range of 10° to 80° with a step size of 0.02° and a scan speed of 2° min<sup>-1</sup>. The surface morphology of nanohybrids was determined using a scanning electron microscope (SEM) (Carl ZEISS EVO 18 Research), and elemental mapping was obtained using energy dispersive X-ray spectroscopic analysis (EDAX). The morphology of the samples was further observed using the transmission electron microscope (TEM) FEI Tecnai F20 Super-Twin equipped with a FEG source (200 kV). The cation concentration in the samples was analyzed using an inductively coupled plasma-mass spectrometer (Agilent 7900-ICP-MS with ASX-500 series ICP-MS autosampler) to investigate the percentages of each element present in the lixivium, synthesized nanohybrids and plant nodes sterilized water. The elemental composition of raw ilmenite and synthesized nanohybrid samples were studied using X-ray fluorescence spectroscopic analysis (XRF). HORIBA Scientific XGT-5200 with an Rh anode X-ray tube at 50 kV and 1 mA current was used. Thermo Scientific Nicolet S10 with attenuated total reflectance (ATR) attachment was used to obtain the Fourier transmission infrared (FTIR) spectroscopy data of the samples. Thermo Scientific ESCALAB Xi+ fitted with Al K $\alpha$  (1486.68 eV) X-ray photoelectron spectroscopy (XPS) analysis was used to collect elemental binding energy data of the synthesized nanohybrids. Diffuse

reflectance spectroscopy (DRS) data was obtained by using the LAMBDA 365 spectrometer to calculate the band gap energy ( $E_g$ ) of synthesized nanohybrids. The Kubelka–Munk equation was used to quantify the BG of FeTiO<sub>3</sub>/TiO<sub>2</sub> and Ag-FeTiO<sub>3</sub>/TiO<sub>2</sub> using Equation (1). The Tauc plot of the nanohybrid was obtained by plotting,  $[F(R) \times h\nu]^n$  versus photon energy ( $h\nu$ ). The direct  $E_g$  was calculated by substituting ( $n$ ) as 2,<sup>[33]</sup> where  $F(R)$ -Kubelka–Munk function.

$$[F(R) \times h\nu]^n = \left( \frac{(1-R)^2}{2R} \times h\nu \right)^n \quad (1)$$

The  $E_g$  of nanohybrids was determined by plotting a tangent line parallel to the x-axis in the exponential curve obtained from  $[F(R) \times h\nu]^2$  versus  $h\nu$ . The intersection point (x-axis) determines the BG value of synthesized samples.

#### 2.5. Plant Tissue Sterilization Experiment

Ornamental plant *D. sanderiana* Sander (“White”) ex Mast nodes were selected as the explant (mother plant tissues) and  $\approx 1$  cm segments were used in this study. For explant sterilization, 150–160 nodes (Nodes per 1 cycle), were thoroughly washed with distilled water for 5 min, then they were placed in a beaker with 100 mL DI water with 1–2 drops of liquid soap and vigorously agitated for 30 min using an orbital shaker at 180 rpm, then drained off the soapy water and washed with sterilized water to remove excess soap from plant tissues. Finally, the following procedure was used sequentially to sterilize the plant nodes. FeTiO<sub>3</sub>/TiO<sub>2</sub>, Ag-FeTiO<sub>3</sub>/TiO<sub>2</sub>, FeTiO<sub>3</sub>, and TiO<sub>2</sub> (20 mg each) were added separately to 100 mL of DI water contained in a 250 mL beaker. Then, 10–12 plant nodes were added to each beaker and mounted on a magnetic stirrer precisely below 50 cm from the light (50 W Warm white LED) surface to achieve an illumination intensity of about  $\approx 8,500$ – $9,000$  Lux (TECPEL DLM 531) inside a sealed chamber (Figure S2,

Supporting Information). Nodes and nanohybrid particle solution were exposed to VL, for 30 min while continuously stirring at a speed of 600 rpm. Sterilized nodes were cultured in Murashige & Skoog medium<sup>[34]</sup> (Figure S10, Supporting Information). Ten culture tubes were accommodated for this experiment. Cultured tubes were kept inside the growth room at 25 °C and illuminated for 14 h per day with a 1500 Lux LED. The nanohybrid was reused two times to assess the efficiency of the material and each time recovered by drying the mixture at 120 °C for 5 h.

As one of the control experiments (Control), 10% (v/v) Clorox (prepared by mixing 20 mL Clorox solution with 180 mL DI water) was used for sterilization of nodal explants. Plant nodes were soaked for 15 min in 100 mL of 10% (v/v) Clorox solution with two drops of liquid soap by agitating the mixture at 180 rpm in an orbital shaker. This washing mixture was decanted and repeated the washing step for nodal explants by soaking in 100 mL of fresh 10% (v/v) Clorox for 15 min and agitating. The solution was then discarded (Important: Clorox could not be reused multiple times). Then the nodes were rinsed thoroughly three times with sterilized water (autoclaved water). After that, the inoculated explants were kept in the same conditions as previously mentioned.

For all sterilizing treatments, the number of cultures free from microbial contaminations (%) was recorded over a period of 30 days in order to study the efficiency of the photocatalytic sterilization technique. Fungal species that severely damaged *D. sanderiana* explant when introduced to the in vitro environment were cultured and observed using an optical microscope (physical characteristics) and by compared with standard fungi.<sup>[35,36]</sup>

Agar was used as growing media to culture the plant nodes. Culturing agar media was prepared using combining Murashige & Skoog medium<sup>[34]</sup> with 3% sugar, 1 mg L<sup>-1</sup> benzyl amino purine (BAP) and then pH was adjusted to 5.8. The chemical mixture was then boiled for 2–3 min at 100 °C in a microwave oven (LG, Microwave radiation-2450 MHz, 1200 W) to melt the agar. The culture tubes and caps were sterilized using 5% (v/v) Clorox, a sterilization technique known as CSUP technique,<sup>[4]</sup> and 5 mL of agar media were poured into the tubes and sealed the cap. Similarly, 1 L of agar media solution was prepared and poured into 200 tubes. The tubes were kept at room temperature (25 °C) to solidify the agar media.

## 2.6. Establishment of Photocatalytic Behavior of Nanohybrid using *Fusarium* spp

According to the microscopic observations of cultured fungal species taken from in vitro established dracaena nodal cultures the fungus was identified as *Fusarium* spp. Hence, two experiments were executed using *Fusarium* spp. isolated from infected *Dracaena* in vitro culture and a standard *F. oxysporum* obtained from the Department of Agriculture, Sri Lanka. The cultures were kept under ≈8,500–9,000 Lux and in total darkness in the presence of the nanohybrid and a control experiment was carried out without the presence of the nanohybrid. Two Ag-FeTiO<sub>3</sub>/TiO<sub>2</sub> and two FeTiO<sub>3</sub>/TiO<sub>2</sub> nanohybrid solutions, each 20 mg/100 mL (200 mg L<sup>-1</sup>) concentration, were

prepared in sterilized deionized distilled water. All solutions were inoculated with an equal amount of *Fusarium* cultures and two were kept under ≈8,500–9,000 Lux and the other two in total darkness while stirring at 600 rpm on a magnetic stirrer for 30 min. Then, the solution of 1 mL, each from these four treatments, was inoculated onto a PDA agar medium. The experiments were replicated five times. All cultures were kept in an incubator at 30 °C and observed the time taken to grow the fungi. Images were taken when the fungi first appeared on each petri dish. All experiments were continued for up to 20 days.

## 2.7. Statistical Analysis

The experimental samples were arranged using a complete randomized design (CRD), and each treatment was repeated thrice. Survival data were analyzed from ANOVA using IBM SPSS ver. 20 program.

## 3. Results and Discussion

Here, we developed a visible light active photocatalyst using locally available ilmenite as a feedstock. The elemental composition of natural ilmenite is given in Table 1.<sup>[37]</sup> Traditional routes to manipulate the band gap of TiO<sub>2</sub>, involve structural modification of the pure TiO<sub>2</sub> extracted from natural feedstocks. In contrast, the pathway reported here allows engineering visible light active hybrids without the need for extraction and purification of TiO<sub>2</sub>.<sup>[38,39]</sup> Microwave digestion technique facilitated the formation of FeTiO<sub>3</sub>/TiO<sub>2</sub> nanohybrid without the need for isolation of TiO<sub>2</sub> using traditional approaches.<sup>[40]</sup>

Ilmenite forms Ti complexes with Cl<sup>-</sup> ions (TiOCl<sub>4</sub><sup>2-</sup>), TiOCl<sub>2</sub>, and TiCl<sub>4</sub>, as well as Fe<sup>2+</sup> and Fe<sup>3+</sup> ions during the initial digestion step.<sup>[40,41]</sup> Pseudo rutile (Fe<sub>2</sub>Ti<sub>3</sub>O<sub>9</sub>) dissolves in concentrated HCl to produce TiO<sup>2+</sup> and Fe<sup>3+</sup> ions, and convert to ferric chloride.<sup>[42]</sup> Furthermore, iron oxide (magnetite) dissolves and forms Fe<sup>2+</sup> and Fe<sup>3+</sup> ions, and makes complexes with Cl<sup>-</sup> ions.<sup>[43]</sup> At this stage, the color of the acid changes from colorless to reddish-brown due to high Fe<sup>3+</sup> concentration.<sup>[42]</sup> Fe<sup>3+</sup> forms an iron chloride (FeCl<sub>4</sub><sup>-</sup>) complex with chloride ions, which stabilizes Fe<sup>3+</sup> ions at very low pH levels.<sup>[41]</sup> The Fe<sup>2+</sup> ions quickly react with OH<sup>-</sup> ions to form stable greenish ferrous hydroxide (Fe(OH)<sub>2</sub>), and by adding dilute HNO<sub>3</sub> at a later stage, most of the Fe(OH)<sub>2</sub> is oxidized into Fe<sup>3+</sup> ion.<sup>[22,44]</sup> A considerable amount of rutile mineral also dissolves in conc. HCl under high temperature, which helps to increase Ti<sup>4+</sup> ion concentration.<sup>[45]</sup> The best solid-to-liquid (acid) ratio S/L ratio to obtain maximum Ti<sup>4+</sup> and Fe<sup>3+</sup> quantity in the extraction process was found to be 1:20 at a temperature of 110 °C, and the leaching time of 1 h leading to the formation of high-quality FeTiO<sub>3</sub>/TiO<sub>2</sub>.<sup>[46]</sup> During the neutralization and hydroxylation of the liquid, the resulting brown color residue contains a mixture of Fe<sup>3+</sup>-H<sub>2</sub>TiO<sub>3</sub>, Fe<sup>2+</sup>-H<sub>2</sub>TiO<sub>3</sub>, Fe(OH)<sub>3</sub>, and Fe<sub>2</sub>Ti<sub>3</sub>O<sub>9</sub>.<sup>[30,31]</sup> The addition of NaOH to the hydrated TiO<sub>2</sub> particles results in the formation of a disordered Na<sub>x</sub>Ti(O<sub>2</sub>)<sub>y</sub>(OH)<sub>z</sub> complexes, Na<sub>2</sub>Ti<sub>3</sub>O<sub>7</sub> and Na<sub>2</sub>TiO<sub>3</sub>.<sup>[47]</sup> Also, NaCl is generated due to unremoved Cl<sup>-</sup> in the residue. Fe<sup>3+</sup> and Fe<sup>2+</sup> then interact with TiO<sup>2+</sup> ions to

form Fe<sup>3+</sup> and Fe<sup>2+</sup> doped TiO<sub>2</sub> nanohybrid. In order to control the particle size of the nanohybrid, the dropping rate of NaOH was controlled at 0.5 mL min<sup>-1</sup>. Continuous stirring was essential to have a homogeneous mixture and to accelerate the reactions. The dilute HNO<sub>3</sub> washing step was essential to leach out the maximum amount of Cl<sup>-</sup> ions and helps to oxidize free Fe<sup>2+</sup> to Fe<sup>3+</sup> ions.<sup>[48]</sup> With the addition of H<sup>+</sup> to the residue, all disordered Na-titanate complex transfers to H<sub>2</sub>TiO<sub>3</sub> and H<sub>2</sub>Ti<sub>3</sub>O<sub>7</sub>, ultimately transforming into an amorphous anatase phase.<sup>[40]</sup>

Silver ion (Ag<sup>+</sup>) was immediately added to the residue with ultrasonication in order to minimize the agglomeration of the nanoparticles, resulting in a well-dispersed homogeneous product. The calcination at 400 °C, results in the formation of a well-crystalline Ag-FeTiO<sub>3</sub>/TiO<sub>2</sub> nanohybrid. The yield of nanohybrid obtained from this method was ≈60% (w/w). Ti species (H<sub>2</sub>TiO<sub>3</sub>, H<sub>2</sub>Ti<sub>3</sub>O<sub>7</sub>) and Fe(OH)<sub>3</sub> particles are converted into anatase (TiO<sub>2</sub>) and hematite (Fe<sub>2</sub>O<sub>3</sub>), respectively during the thermal treatment at a mild annealing temperature of 400 °C.<sup>[31]</sup> These observations are supported by the characterization results explained below. The interactions of Ag with FeTiO<sub>3</sub> and TiO<sub>2</sub> result in the formation of the Ag-FeTiO<sub>3</sub>/TiO<sub>2</sub> and FeTiO<sub>3</sub>/TiO<sub>2</sub> nanohybrids. In addition to the presence of small amounts of oxygen and high-temperature calcination, Ag<sub>2</sub>O can be generated as a minor phase.<sup>[49]</sup> Also, some Ag<sub>2</sub>O converts to Ag elements at high temperatures.<sup>[50]</sup>

### 3.1. Characterization of Ag-FeTiO<sub>3</sub>/TiO<sub>2</sub> and FeTiO<sub>3</sub>/TiO<sub>2</sub> Nanohybrids

Figure 1a summarizes the synthesis pathway of Ag-decorated iron titanate/titanium dioxide nanohybrids. PXRD patterns of FeTiO<sub>3</sub>/TiO<sub>2</sub> and Ag-FeTiO<sub>3</sub>/TiO<sub>2</sub> nanohybrids are shown in Figure 1b. FeTiO<sub>3</sub> and the anatase form of TiO<sub>2</sub> are identified as the major crystalline phases. Previous reports also suggest that TiO<sub>2</sub> obtained via acid-hydrolysis generates an anatase phase rather than rutile with low calcination temperatures (<600 °C).<sup>[23]</sup> PXRD diffractogram of silver decorated sample shows additional three peaks for Ag<sup>0</sup> (JCPDS PDF# 01-087-0597), Ag<sub>2</sub>O (JCPDS PDF# 00-001-1041). Here, the Ag ion does not enter into the lattice of FeTiO<sub>3</sub>/TiO<sub>2</sub> crystal during the calcination process due to the higher ionic radii of Ag<sup>+</sup> (1.15 Å) compared to Ti<sup>4+</sup> (0.60 Å). Results suggest that Ag decorates the surfaces of FeTiO<sub>3</sub> and TiO<sub>2</sub>. Furthermore, both FeTiO<sub>3</sub>/TiO<sub>2</sub> and Ag-FeTiO<sub>3</sub>/TiO<sub>2</sub> contained hematite (Fe<sub>2</sub>O<sub>3</sub>) (JCPDS PDF# 01-072-0469), iron titanate (FeTiO<sub>3</sub>) (JCPDS PDF# 01-075-1212) and pseudorutile (Fe<sub>2</sub>Ti<sub>3</sub>O<sub>9</sub>) (JCPDS PDF# 00-029-1494) phases.

SEM analysis indicates significant changes in grain sizes and shapes, when ilmenite (Figure S1, Supporting Information) transforms into calcined FeTiO<sub>3</sub>/TiO<sub>2</sub> (Figure S3i, Supporting Information) and Ag-FeTiO<sub>3</sub>/TiO<sub>2</sub> (Figure S3ii, Supporting Information) nanohybrids. It clearly shows the disorganized macro nature of the natural ilmenite particles which are in non-uniform size and the aggregation of particles in the nanohybrid. The morphology of synthesized particles was of uneven size and different shapes due to the aggregation nature. The elemental composition present in FeTiO<sub>3</sub>/TiO<sub>2</sub> and Ag-FeTiO<sub>3</sub>/TiO<sub>2</sub> was determined using ray EDAX. The findings revealed the presence of a minor amount of unreacted Cl<sup>-</sup> ions.

FeTiO<sub>3</sub>/TiO<sub>2</sub> contained Fe (35.38%), Ti (34.88%), O (28.92%), Cl (0.82%), and Ag-FeTiO<sub>3</sub>/TiO<sub>2</sub> contained Fe (35.01%), Ti (34.59%), O (26.96%), Cl (0.72%), and Ag (2.72%) as determined using EDX.

TEM images were used to examine the morphology, particle size, and particle size distribution of the Ag-FeTiO<sub>3</sub>/TiO<sub>2</sub> and FeTiO<sub>3</sub>/TiO<sub>2</sub> nanoparticles, as shown in Figure 2a–f. Figure 2a–d shows the 50 nm scale TEM images of Ag-FeTiO<sub>3</sub>/TiO<sub>2</sub> and FeTiO<sub>3</sub>/TiO<sub>2</sub>. According to TEM analysis, nanohybrid particles have irregular morphology. Moreover, in Figure 2b, it can be found that silver and silver oxide nanoparticles structurally are in contact with the FeTiO<sub>3</sub>/TiO<sub>2</sub>. Such morphological hierarchy enables to create the heterojunction interfaces in the Ag-FeTiO<sub>3</sub>/TiO<sub>2</sub> nanohybrid. Figure 2c,f revealed that average crystal size of the Ag-FeTiO<sub>3</sub>/TiO<sub>2</sub> and FeTiO<sub>3</sub>/TiO<sub>2</sub> nanohybrids are approximately 4.2–6.6 nm (SD = ±0.215) and 3.5–9.2 nm (SD = ±0.372), respectively.

Also, Figure 2e shows, anatase particles are contacted with iron titanate nanoparticles to promote electron transitions efficiently. Hence, these morphological modifications efficiently promote the charge separation and migration of photo-induced electron-hole pairs in the as-synthesized Ag-FeTiO<sub>3</sub>/TiO<sub>2</sub> and FeTiO<sub>3</sub>/TiO<sub>2</sub>, which enables it to absorb visible light from the solar spectrum.

Selected area electron diffraction (SAED) patterns of Ag-FeTiO<sub>3</sub>/TiO<sub>2</sub> and FeTiO<sub>3</sub>/TiO<sub>2</sub>, respectively are shown in Figure S4, Supporting Information. The observations suggest the presence of polycrystalline planes in both nanohybrids.

The chemical interaction of the nanohybrid was further explored using XPS spectroscopy. The survey spectra of FeTiO<sub>3</sub>/TiO<sub>2</sub> confirm the presence of Fe 2p, O 1s, Ti 2p, and C 1s while the presence of Fe 2p, O 1s, Ti 2p, C 1s, and Ag 3d bands were observed in the Ag-FeTiO<sub>3</sub>/TiO<sub>2</sub> nanohybrid. More details on high-resolution XPS spectra of both nanohybrids are presented in supporting information (Figure S5, Supporting Information) and the atomic concentration of each element is summarized in Table 2.

As shown in Figure 3b–d, the peak shift of Fe 2P<sub>3/2</sub> (0.19 eV), Ti (0.07 eV), and O 1s (0.13 eV), towards lower binding energy (BE) values in Ag-FeTiO<sub>3</sub>/TiO<sub>2</sub> nanohybrid, is observed compared to the FeTiO<sub>3</sub>/TiO<sub>2</sub> nanohybrid. These observations suggest favorable interaction between the nanohybrid and Ag phase after introducing Ag<sup>+</sup> to FeTiO<sub>3</sub>/TiO<sub>2</sub> nanohybrid.

The high-resolution spectra of Fe (Figure 3b) in Ag-FeTiO<sub>3</sub>/TiO<sub>2</sub> show two significant peaks for 2p<sub>3/2</sub> and 2p<sub>1/2</sub> electron spins at 711.09 and 724.77 eV, respectively. At the same time, Fe in the FeTiO<sub>3</sub>/TiO<sub>2</sub> nanohybrid shows dominant peaks at 711.28 eV for 2p<sub>3/2</sub> and 724.96 eV for Fe 2p<sub>1/2</sub> electrons (Figure 3b). The minor binding energy shifts of Fe 2p confirm the change of chemical environment in FeTiO<sub>3</sub>/TiO<sub>2</sub> after the introduction of Ag to the matrix. In addition, the XPS spectrum of Ti in Ag-FeTiO<sub>3</sub>/TiO<sub>2</sub> shows peaks at 458.54 and, 464.32 eV and they correspond to the BE of Ti 2p<sub>3/2</sub> and 2p<sub>1/2</sub> electrons while the BE peaks at 458.61 and 464.32 eV are corresponding to the Ti 2p<sub>3/2</sub> and 2p<sub>1/2</sub> electrons in the FeTiO<sub>3</sub>/TiO<sub>2</sub> nanohybrid, determined as Ti<sup>4+</sup> ion in TiO<sub>2</sub> (anatase) matrix (Figure 3c).

The XPS spectrum of O 1s in Ag-FeTiO<sub>3</sub>/TiO<sub>2</sub> nanohybrid is presented in Figure 3d. The intensive BE peaks of O 1s in Ag-FeTiO<sub>3</sub>/TiO<sub>2</sub> are observed at 530.06 eV while BE peaks of

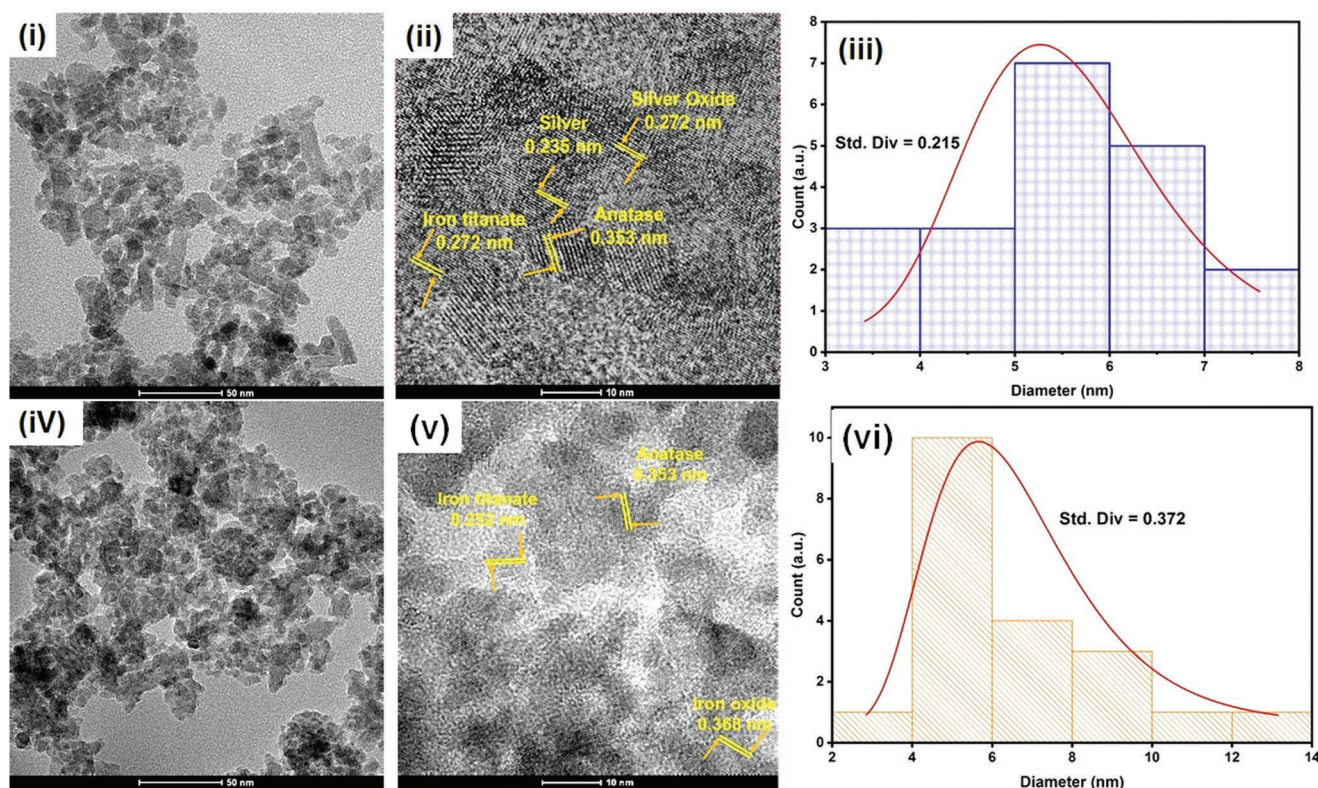


**Figure 2.** i) TEM image of Ag-FeTiO<sub>3</sub>/TiO<sub>2</sub> at 50 nm scale, ii) lattice planes of Ag-FeTiO<sub>3</sub>/TiO<sub>2</sub>, iii) average particle size distribution of Ag-FeTiO<sub>3</sub>/TiO<sub>2</sub>, iv) TEM image of FeTiO<sub>3</sub>/TiO<sub>2</sub> at 50 nm scale, v) lattice planes of FeTiO<sub>3</sub>/TiO<sub>2</sub>, and vi) average particle size distribution of FeTiO<sub>3</sub>/TiO<sub>2</sub>.

O 1s in FeTiO<sub>3</sub>/TiO<sub>2</sub> are observed at 530.19 eV (Figure 3d). The Ag XPS analysis revealed two peaks of Ag in Ag-FeTiO<sub>3</sub>/TiO<sub>2</sub> nanohybrid at 367.48<sup>[51]</sup> and 373.45 eV<sup>[52,53]</sup> which are corresponding to the 3d<sub>5/2</sub> and 3d<sub>3/2</sub> electrons. There is a significant shift in the Ag peaks compared to standard binding energies of Ag, 368.2 eV for 3d<sub>5/2</sub> and Ag<sup>+</sup>, 367.9 eV for 3d<sub>5/2</sub> suggesting electron density change when Ag<sup>0</sup> and Ag<sub>2</sub>O interacted with FeTiO<sub>3</sub>/TiO<sub>2</sub>. According to previous studies, Ag<sup>0</sup> improves plasmonic absorption and thereby reduces the BG.<sup>[19,54,55]</sup>

DRS technique was used to calculate the optical BG of FeTiO<sub>3</sub>/TiO<sub>2</sub> and Ag-FeTiO<sub>3</sub>/TiO<sub>2</sub> nanohybrids (see Figure 4a,b). The calculated E<sub>g</sub> of FeTiO<sub>3</sub>/TiO<sub>2</sub> and Ag-FeTiO<sub>3</sub>/TiO<sub>2</sub> are 2.94 and 2.80 eV, respectively. FeTiO<sub>3</sub>/TiO<sub>2</sub> and Ag-FeTiO<sub>3</sub>/TiO<sub>2</sub> nanohybrids have much lower BG than pristine anatase (3.2 eV). The presence of Fe<sub>2</sub>O<sub>3</sub>, Ag<sub>2</sub>O, and Ag<sup>0</sup> significantly lowered the BG of anatase while scavenging energized electrons generated by TiO<sub>2</sub>.<sup>[18,51]</sup> In addition, Fe<sup>3+</sup> doped TiO<sub>2</sub> also reduces the BG due to the insertion of impurity energy levels.<sup>[56,57]</sup> Previous studies suggest that Fe impurity energy levels are mostly present at lower CB positions than TiO<sub>2</sub>, thus electron-hole pair recombination rate of TiO<sub>2</sub> is reduced.<sup>[22,23]</sup>

The presence of Ag species (Ag<sup>0</sup> and Ag<sub>2</sub>O) on the surface of FeTiO<sub>3</sub>/TiO<sub>2</sub> further lowers the BG than FeTiO<sub>3</sub>/TiO<sub>2</sub>. Ag has a higher attraction to scavenge energized electrons than Fe and thus it offers added advantages in photocatalytic efficacy.<sup>[56]</sup> Moreover, the absorption wavelength of Ag-FeTiO<sub>3</sub>/TiO<sub>2</sub> was shifted towards a higher wavelength (518.20 nm) compared to FeTiO<sub>3</sub>/TiO<sub>2</sub> (see Figure 4). It is concluded that the presence of both Fe<sub>2</sub>O<sub>3</sub> and Ag<sup>0</sup>/Ag<sub>2</sub>O species on the Ag-FeTiO<sub>3</sub>/TiO<sub>2</sub> surface leads to improved visible light catalytic activity.

The structural features of Ag-FeTiO<sub>3</sub>/TiO<sub>2</sub> and FeTiO<sub>3</sub>/TiO<sub>2</sub> nanohybrids were further investigated using the FTIR technique (see Figure 5). The narrow peak centered around 3438 cm<sup>-1</sup> is associated with the stretching vibrations of O–H and the frequency is significantly broadened (3400–3600 cm<sup>-1</sup>) in Ag-FeTiO<sub>3</sub>/TiO<sub>2</sub> after the incorporation of Ag. Such peak broadening is an indication of strong interactions due to the presence of different strengths of O–H vibrations. This observation is further attested by the minor shift in the bending modes of O–H bonds appearing at 1630 and 1634 cm<sup>-1</sup> attributed to bending vibration in adsorbed water, similar peak values obtained for previous reports as well.<sup>[18,23,58]</sup> The C–H

**Table 2.** XPS elemental binding energy peaks and their atomic concentration (%) of each element in Ag-FeTiO<sub>3</sub>/TiO<sub>2</sub> and FeTiO<sub>3</sub>/TiO<sub>2</sub> nanohybrids.

Material	Ti		Fe		O		Ag	
	Ti 2p [eV]	%	Fe 2p [eV]	%	O 1s [eV]	%	Ag 3d [eV]	%
FeTiO <sub>3</sub> /TiO <sub>2</sub>	458.55	10.26	711.18	3.89	529.40	44.52	–	–
Ag-FeTiO <sub>3</sub> /TiO <sub>2</sub>	458.60	9.35	711.24	3.22	529.91	40.30	367.20	0.41

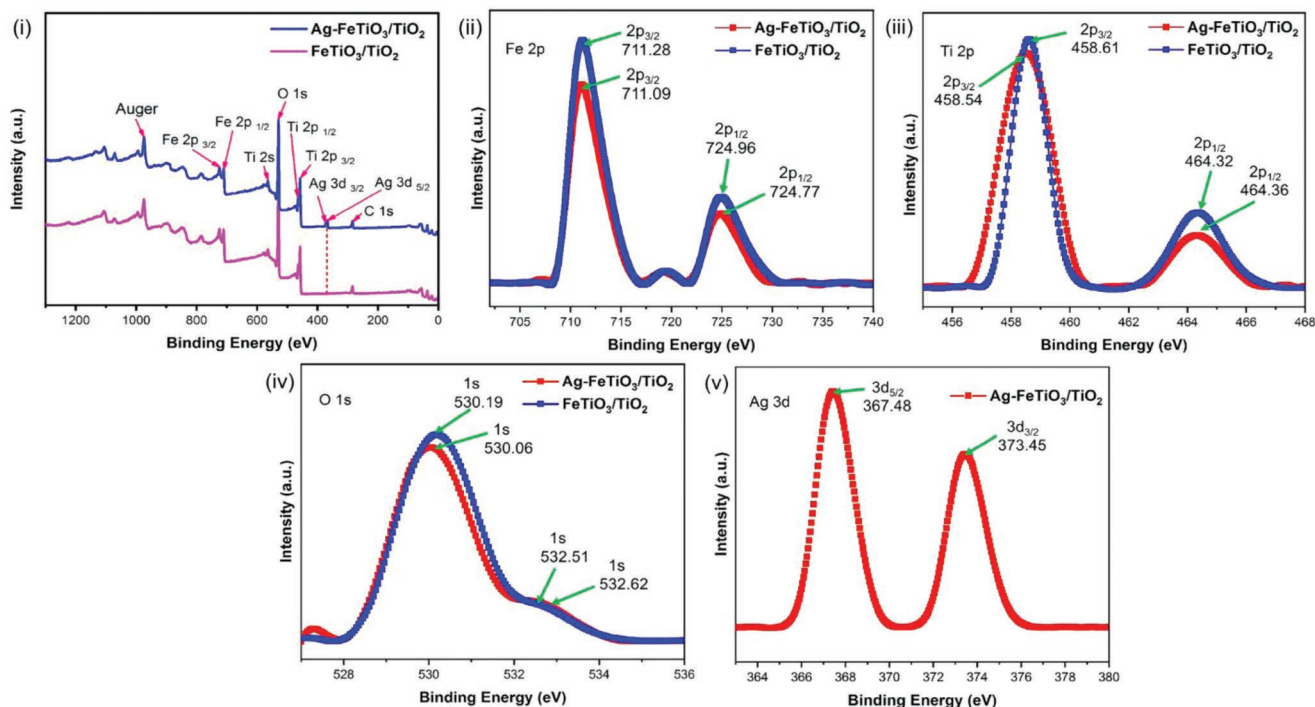


**Figure 3.** i) Survey XPS spectrum of Ag-FeTiO<sub>3</sub>/TiO<sub>2</sub> and FeTiO<sub>3</sub>/TiO<sub>2</sub>, Stacked binding energy spectra of ii) Fe, iii) Ti, and iv) O elements in Ag-FeTiO<sub>3</sub>/TiO<sub>2</sub> and FeTiO<sub>3</sub>/TiO<sub>2</sub> and v) XPS spectra of Ag for Ag-FeTiO<sub>3</sub>/TiO<sub>2</sub>.

stretching vibration appeared at 1384 cm<sup>-1</sup> in an alkane and also appears in both nanohybrids.<sup>[59]</sup> In 1122 cm<sup>-1</sup> band identified as C–N stretching vibration present in both nanohybrids. Thus, suggesting nanohybrids contain some nitrogen complexes due to heating under N<sub>2</sub> gas. Such peaks are not observed in the FeTiO<sub>3</sub>/TiO<sub>2</sub> hybrid before heating. The metal oxides fingerprint region was identified around the 400–600 cm<sup>-1</sup> range. FeTiO<sub>3</sub>/TiO<sub>2</sub> nanohybrid shows 517 cm<sup>-1</sup> wavenumber while Ti–O bond value for pure TiO<sub>2</sub> is 460 cm<sup>-1</sup>. Due to the presence

of Fe–O (probably Fe<sub>2</sub>O<sub>3</sub>) in the nanohybrid, the Ti–O band value shifted to a higher range. This was suggested by the previous report also.<sup>[60]</sup> Moreover, Ag-FeTiO<sub>3</sub>/TiO<sub>2</sub> shows a Ti–O band at 601 cm<sup>-1</sup>, due to the interaction of Ag, Fe<sub>2</sub>O<sub>3</sub> with TiO<sub>2</sub>. Thus, the observations confirm the presence of Ag in FeTiO<sub>3</sub>/TiO<sub>2</sub> nanohybrid changes the chemical structure.<sup>[24,33,44]</sup>

XRF study shows the elemental composition of FeTiO<sub>3</sub>/TiO<sub>2</sub> and Ag-FeTiO<sub>3</sub>/TiO<sub>2</sub> nanohybrids. The FeTiO<sub>3</sub>/TiO<sub>2</sub> nanohybrid comprises Fe (53.14%) (w/w), Ti (44.38%) (w/w), Cr

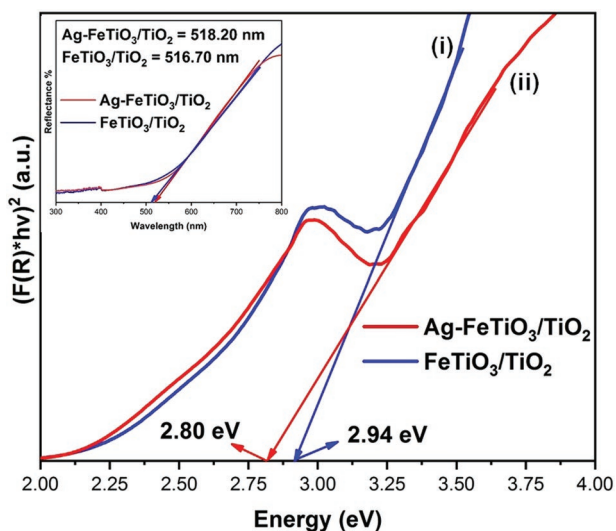


**Figure 4.** DRS spectra of i) FeTiO<sub>3</sub>/TiO<sub>2</sub> and ii) Ag-FeTiO<sub>3</sub>/TiO<sub>2</sub> nanohybrids.

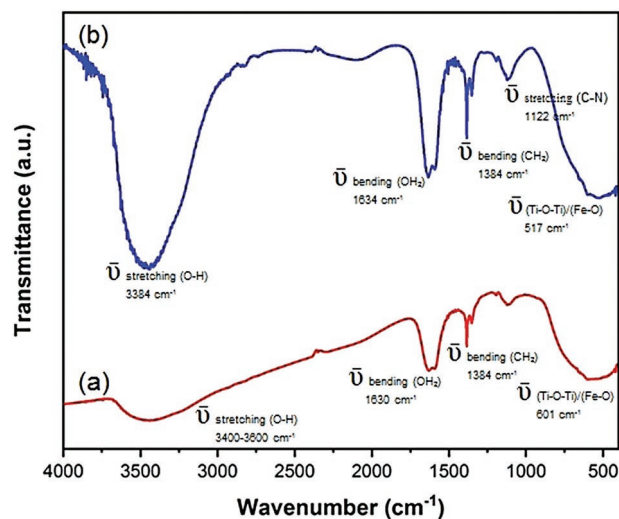


**Figure 5.** FTIR spectra of a) Ag-FeTiO<sub>3</sub>/TiO<sub>2</sub> and b) FeTiO<sub>3</sub>/TiO<sub>2</sub> nanohybrids.

**Table 3.** Elemental composition in lixivium, nanohybrids, and washed water.

Liquid phase	Concentration [RSD] <sup>a)</sup> /ppm]				
	Ti	Fe	Ag	Cr	Mn
Lixivium	3974.27 (9.39)	10,663.88 (21.34)	–	70.36 (13.73)	631.56 (27.14)
Ag-FeTiO <sub>3</sub> /TiO <sub>2</sub>	51.37(0.62)	188.77 (2.86)	9.68 (4.05)	1.38 (2.09)	2.42 (3.09)
FeTiO <sub>3</sub> /TiO <sub>2</sub>	66.32 (0.30)	195.56 (3.29)	–	2.95 (2.22)	9.72 (3.41)
Washing water					
1 <sup>st</sup> wash	0.08 (0.03)	2.16 (0.09)	0.03 (0.01)	0.13 (0.04)	0.24 (0.08)
2 <sup>nd</sup> wash	0.23 (0.06)	1.80 (0.12)	0.05 (0.01)	0.12 (0.08)	0.39 (0.13)
3 <sup>rd</sup> wash	0.45 (0.12)	1.34 (0.05)	0.46 (0.02)	0.05 (0.02)	0.25(0.04)

<sup>a)</sup>Relative Standard Deviation in ppm indicates in the brackets; detection limits (DL) for Ti = 0.1 ppb, Fe = 1 ppb, Ag = 0.1 ppb, Cr = 0.1 ppb, and Mn = 0.1 ppb<sup>[61]</sup>

(0.83%), and Mn (1.65%). Ag-FeTiO<sub>3</sub>/TiO<sub>2</sub> shows Fe (53.20%) (w/w), Ti (43.45%) (w/w), Cr (0.1%) (w/w), Mn (0.83%) (w/w), and Ag (2.42%) (see Figure S6, Supporting Information).

Furthermore, quantitative analysis was carried out using ICP-MS (Table 3). According to ICP-MS data, the element ratio of Fe/Ti was 2.68 in the lixivium. The nanohybrids show less Fe and Ti concentrations than lixivium.

### 3.2. Antimicrobial Activity Studies using *D. Sanderiana* Plant Tissues

A common fungi contamination by *Fusarium* spp. (see Figure 6) is one of the major challenges in tissue culture propagation



**Figure 6.** Fungal growth (*Fusarium* spp.) grown in culture media of *Dracaena sanderiana* plant tissues (Red color arrow indicates the fungus).

of the ornamental plant *D. sanderiana*.<sup>[27]</sup> We obtained healthy plant nodes free from microbial contaminations by sterilizing nodes using nanohybrids as the sterilizing agent for 1 month period (see Figure S11, Supporting Information).

The findings indicated, that 18 out of 20 dracaena nodes survived when Ag-FeTiO<sub>3</sub>/TiO<sub>2</sub> nanohybrid was used for two washing cycles. Also, six nodes survived the third wash as well. Thus, Ag-FeTiO<sub>3</sub>/TiO<sub>2</sub> nanohybrid was able to survive 24 out of 30 plant nodes from the first trial. FeTiO<sub>3</sub>/TiO<sub>2</sub> nanohybrid survived 18 out of 30 nodes. In this experiment, 10% Clorox, ilmenite, and TiO<sub>2</sub> nanomaterials showed survival in 16, 9, and 9 out of 30 nodes, respectively (see Figure 7a). Thus, it can be stated that Ag-FeTiO<sub>3</sub>/TiO<sub>2</sub> nanohybrid sterilization technique produces more promising results than other nanomaterials.

It was observed that the highest percentage of survival of nodes was observed when Ag-FeTiO<sub>3</sub>/TiO<sub>2</sub> was used for sterilization, see Figure 7b. The observation confirms the enhanced photocatalytic activity of the nanohybrid under visible light. The potential for the re-use of nanohybrid was evaluated. The findings indicated that 90% of plant nodes survived after two washing cycles when Ag-FeTiO<sub>3</sub>/TiO<sub>2</sub> was used and 60% of plant nodes survived after the third washing cycle. In comparison, FeTiO<sub>3</sub>/TiO<sub>2</sub> nanohybrid is able to survive 80% after the first wash, 60% after the second wash, and 40% after the third wash, respectively.

In comparison, when, the 10% Clorox sterilizing technique was used only 50% of plant nodes survived after the first and the second washings, implying that 10% Clorox cannot degrade fungus/bacteria, effectively. In contrast, FeTiO<sub>3</sub> is able to survive 50% after the first wash, 30% after the second wash, and 10% after the third wash, respectively. Pure TiO<sub>2</sub> nanoparticles are able to survive only 40% after the first wash, 30% after the second wash, and 20% after the third wash, respectively. The observations clearly indicated the effectiveness of Ag-FeTiO<sub>3</sub>/TiO<sub>2</sub> nanohybrid under visible light activation.

We predict that plant node sterilization was caused due to the photocatalytic action of the nanohybrids. The involvement of silver (i.e., Ag<sup>0</sup> and Ag<sub>2</sub>O) improves the sterilization of nodes and allows more nodes to survive than the FeTiO<sub>3</sub>/TiO<sub>2</sub> nanohybrid. Ag-FeTiO<sub>3</sub>/TiO<sub>2</sub> particles demonstrated strong photocatalytic behavior and destroyed microbes on the plant nodes' surface. The presence of Ag enhances the photocatalytic activity



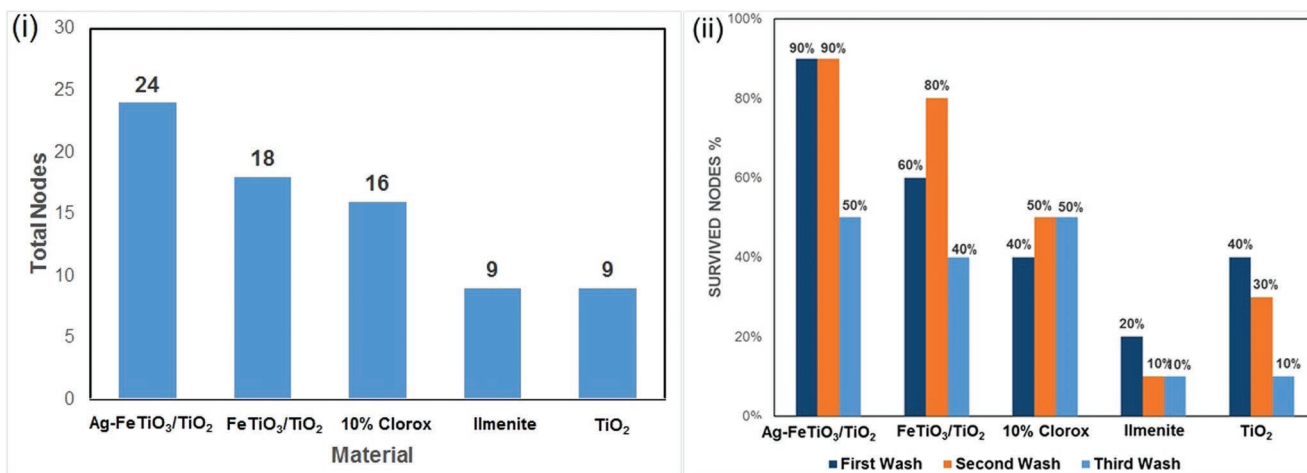


**Figure 7.** i) Total nodes survived after being sterilized using different sterilizing agents. ii) Graph showing the % survival of plant nodes after 1<sup>st</sup>, 2<sup>nd</sup>, and 3<sup>rd</sup> washings.

of FeTiO<sub>3</sub>/TiO<sub>2</sub> while its inherent sterilization ability further improves the efficacy of the nanohybrid.<sup>[11,62]</sup> Such sterilization ability of Ag is explained in previous publications.<sup>[63,64]</sup> Therefore, the use of Ag in plant tissue culture offers advantages like removal of microbial contamination, callus induction, organogenesis, genetic changes, and metabolite synthesis.<sup>[65]</sup> Thus, the introduction of Ag into FeTiO<sub>3</sub>/TiO<sub>2</sub> nanoparticles not only improves the visible light photocatalytic activity of Ag-FeTiO<sub>3</sub>/TiO<sub>2</sub> but also its inherent sterilization effect further improves the properties of the nanohybrid.<sup>[11,64]</sup> As a result, Ag-FeTiO<sub>3</sub>/TiO<sub>2</sub> acts as a strong photocatalyst than FeTiO<sub>3</sub>/TiO<sub>2</sub>.

This experiment was duplicated to determine the reproducibility and efficiency of the photocatalytic sterilization under VL, and the findings did not deviate drastically from the first experiment (Figures S7 and S8, Supporting Information), suggesting the reusability of the photo-catalysts. Furthermore, after the third trial, nanohybrid particles were lost, hence further reuse was not possible. It was found that the particles were removed with plant nodes in each washing cycle (Mass loss- 10% after 1<sup>st</sup> wash, 60% after 2<sup>nd</sup> wash). Clorox is discarded after every washing cycle and generates toxic liquid waste every day with more in vitro plant experiments. Figure S11, Supporting Information shows healthy-grown plant tissues after sterilization from Ag-FeTiO<sub>3</sub>/TiO<sub>2</sub> nanohybrid. These observations confirmed that the nanohybrid is non-toxic to plants, whereas Clorox residues show white burning spots on the plant tissue surface. By applying nanohybrids plant tissues were grown healthy and no further contaminations occurred even after a 1-month period (Figure S11, Supporting Information). However, Clorox treatment shows some fungal contaminations after 1 month. Therefore, this photocatalytic sterilization technique shows excellent disinfection capability against exophytic microbes present in plant tissues.

**Table 4** shows the statistical calculation data of the tissue culture experiments. Results show a significant association between treatment and survival rate ( $p \leq 0.05$ ) according to the statistical analysis results. Results indicate that nanohybrid treatment is highly sufficient for eliminating adhering microbes.

### 3.3. Confirmation of Photocatalytic Behavior of Ag-FeTiO<sub>3</sub>/TiO<sub>2</sub> against *Fusarium* spp

As shown in **Figure 8a** samples kept under visible light with an intensity of  $\approx 8,500$ – $9,000$  Lux illumination did not produce any fungal growth of the *F. oxysporum*, in both the collected fungi from in vitro cultures and the standard species (Figure S9, Supporting Information) of any of the replicates even after 20 days. In contrast, the replicates in the total darkness produced fungal growth after 6 days at 30 °C (Figure 8b). The rate of fungal growth in the sample containing Ag-FeTiO<sub>3</sub>/TiO<sub>2</sub> nanohybrid in dark conditions was relatively slower and less intense. Meanwhile, heavy contaminations were observed in the control samples without the nanohybrid at a high rate even after 3 days. The nanohybrid without silver also demonstrated photocatalytic activity for up to about 8 days as shown in Figure 8c. This observation agrees with the band gap calculations. However, the activity has been significantly improved due to the presence of Ag nanoparticles. The observations confirm that the synergistic effect of Ag and the lowering of the band gap in the nanohybrid ensured enhanced photocatalytic activity.

### 3.4. Proposed Photocatalytic Sterilization Mechanism of Ag-FeTiO<sub>3</sub>/TiO<sub>2</sub> Nanohybrid

The photocatalytic sterilization mechanism (**Figure 9**) is based on oxidation reactions occurring with microbial cells via ROS

**Table 4.** Statistical data analysis of survived nodes.

Treatments <sup>a)</sup>	Survival of nodal explants [mean $\pm$ SD]
Ag-FeTiO <sub>3</sub> /TiO <sub>2</sub>	8.00 $\pm$ 1.73
FeTiO <sub>3</sub> /TiO <sub>2</sub>	6.00 $\pm$ 2.00
10% Clorox	5.33 $\pm$ 0.57
FeTiO <sub>3</sub>	3.00 $\pm$ 2.00
TiO <sub>2</sub>	3.00 $\pm$ 1.00

<sup>a)</sup> Means followed by the same letter within a column are not significantly different at ( $p < 0.05$ ).

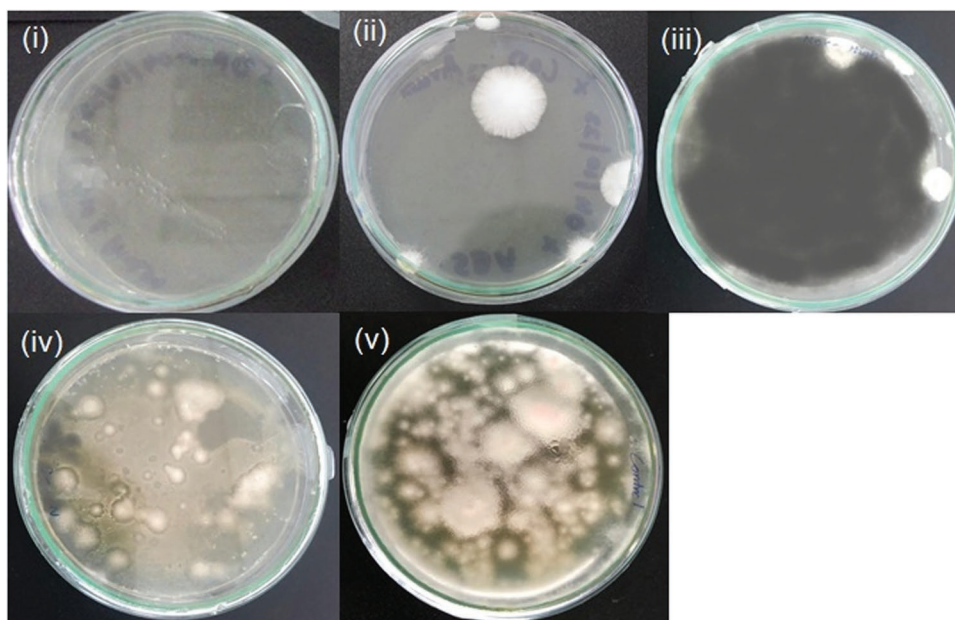


**Figure 8.** Appearance of growth of *Fusarium oxysporum* isolated from in vitro cultures of *Dracaena* i) with Ag-FeTiO<sub>3</sub>/TiO<sub>2</sub> nanohybrid in light, ii) with Ag-FeTiO<sub>3</sub>/TiO<sub>2</sub> nanohybrid in dark, iii) with FeTiO<sub>3</sub>/TiO<sub>2</sub> nanohybrid in light, iv) with FeTiO<sub>3</sub>/TiO<sub>2</sub> nanohybrid in dark, and v) control fungal growth without nanohybrids.

species. The high oxidation power of ROS species leads to the rapid degradation of microbes attached to the surface of the plant node. In the Ag-decorated FeTiO<sub>3</sub>-TiO<sub>2</sub> nanohybrid, the band gap is reduced due to the presence of the impurities such as AgO and Fe<sub>2</sub>O<sub>3</sub> from 3.2 to 2.80 eV. Ag is extensively used as a noble metal dopant. Light exposure leads to the collective oscillation of surface electrons in the metal dopants. This enhances the absorption of visible regions. When metals like Ag and Fe doped to TiO<sub>2</sub>, these metals act as electron donors by supplying the generated electrons to the conduction band

of TiO<sub>2</sub>.<sup>[15,39]</sup> In turn, the holes created on the noble metals due to the plasmonic effect act as effective capturing sites of electrons emitted by the TiO<sub>2</sub> valence band. Thereby suppressing the electron-hole recombination. Formed positive h<sup>vb+</sup> in the valence band reacts with water (H<sub>2</sub>O) or HO<sup>-</sup> to form hydroxyl radicals (OH<sup>·</sup>), hydrogen peroxide (H<sub>2</sub>O<sub>2</sub>), and protonated superoxide radicals (HOO<sup>·</sup>). Collectively these reactive oxidizing species (HO<sup>·</sup>, HO<sub>2</sub><sup>·</sup>, O<sub>2</sub><sup>·-</sup>) and h<sup>vb+</sup>/e<sup>cb-</sup> react with the impurities including organic materials (bacteria, viruses, and other biological materials) leading to complete carbon dioxide and water.<sup>[9,15,66,67]</sup>

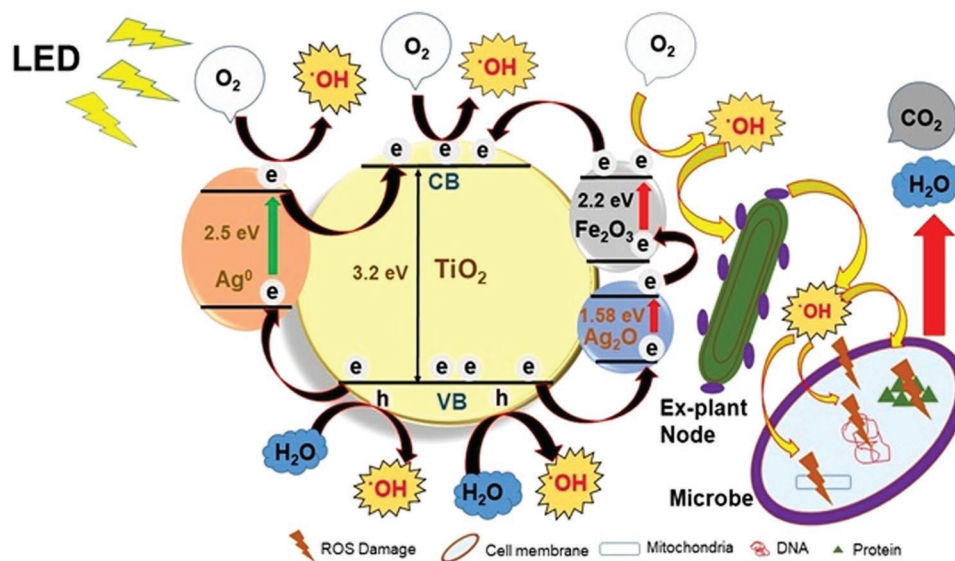


**Figure 9.** Photocatalytic sterilization mechanism of destroying surface adhered microbes in plant node.

## 4. Conclusion

The results confirm the potential of natural ilmenite as a feedstock for the development of visible light-active photocatalysts. Here, the catalytic materials are developed without isolating TiO<sub>2</sub> as was reported before. Decoration of the acid-leached FeTiO<sub>3</sub>/TiO<sub>2</sub> nanohybrid with Ag improves the photon absorption in the visible region significantly by reducing the BG of TiO<sub>2</sub> to the visible region. The photocatalytic properties of the Ag decorated nanohybrid are confirmed by using it as a disinfectant material in developing new plants by tissue culture techniques. The Ag-FeTiO<sub>3</sub>/TiO<sub>2</sub>, shows higher survival percentage (90%) and a longer sterilization period over a month than the traditional Clorox treatment in tissue culture disinfectant applications, suggesting it can be used to sterilize plant tissues in vitro cultures. As a result, this innovative sterilization strategy is a low-cost, eco-friendly, and secure method compared to traditional chemical and physical treatments. The most notable benefit of this method is that hazardous chemicals like mercury chloride (HgCl<sub>2</sub>), and Clorox can be replaced by this nanohybrid. The Clorox cannot be reused, whereas Ag-FeTiO<sub>3</sub>/TiO<sub>2</sub> nanohybrid, can be reused as indicated in our final observations, which is an extra benefit. Finally, we believe that the synthesis method of this novel nanohybrid and photo-sterilization technique is a more beneficial approach in the plant tissue culture industry.

## Supporting Information

Supporting Information is available from the Wiley Online Library or from the author.

## Acknowledgements

This research was financially supported by the Accelerating Higher Education Expansion and Development (AHEAD) Operation of the Ministry of Higher Education Sri Lanka funded by the World Bank with grant number RIC No-01. The authors also thank Lanka Mineral Sands Ltd, Sri Lanka for providing ilmenite samples, the Central Instrument Facility at University of Sri Jayewardenepura for XRD, FTIR, Mr. M.T.M.R. Jayaweera for SEM analysis at the University of Moratuwa, Sri Lanka Institute of Nanotechnology (SLINTEC) for XRF, XPS, and ICP-MS instrumental facilities, Institute of Chemistry Ceylon (IChemC) for Microwave Digester facility and Mr. Akshey Kaushal for TEM analytical service at CRF, IIT (KSB) New Delhi. Ultimately authors thank Ms. Gayani K. Weerakkody (Research Assistant) at SLIIT for conducting tissue culture experiments.

## Conflict of Interest

The authors declare no conflict of interest.

## Author Contributions

N.K., I.M., and S.E.P. developed the idea, supervised the project, involved in data interpretation, obtained the grant, and finalized the manuscript. K.L.S. carried out the experiments, collected data, analyzed and drafted the manuscript. C.N.P. co-supervised the project. P.K. was

involved in data analysis, interpretation, and manuscript drafting. All authors approved the final manuscript.

## Data Availability Statement

The data that support the findings of this study are available from the corresponding author upon reasonable request.

## Keywords

ilmenite, in vitro culture, iron titanate, nanohybrid, photocatalytic sterilization, silver decorated, visible light active

Received: August 7, 2022

Revised: October 26, 2022

Published online:

- [1] R. M. N. T. Amarasinghe, J.-H. Wang, W.-X. Xie, L.-C. Peng, S.-F. Li, H. Li, *Sri Lanka J. Food Agric.* **2018**, *4*, 9.
- [2] I. B. Omamor, A. O. Asemota, C. R. Eke, E. I. Eziashi, *Afr. J. Agric. Res.* **2007**, *2*, 534.
- [3] C. Leifert, J. Y. Ritchie, W. M. Waites, *World. J. Microbiol. Biotechnol.* **1991**, *7*, 452.
- [4] S. E. Peiris, E. D. U. D. De Silva, M. Edussuriya, A. M. U. R. K. Attanayake, B. C. N. Peiris, *J. Natl. Sci. Found. Sri Lanka* **2012**, *40*, 49.
- [5] J. A. T. da Silva, B. Winarto, J. Dobránszki, S. Zeng, *Yuanyi Tongbao* **2015**, *27*, 3.
- [6] S. E. Peiris, H. Hemathilaka, C. N. Peiris, A. W. Wijeratne, in *Proc. of the SLIIT Int. Conf. on Advancements in Sciences and Humanities [SICASH]*, Sri Lanka Institute of Information Technology (SLIIT), Colombo, Sri Lanka **2021**, p. 83–88.
- [7] M. R. Senger, D. B. Rosemberg, K. J. Seibt, R. D. Dias, M. R. Bogo, C. D. Bonan, *Neurotoxicology* **2010**, *31*, 291.
- [8] Y. Takatsuji, S. Ishikawa, T. Haruyama, *Process Biochem.* **2017**, *54*, 140.
- [9] J. Hou, L. Wang, C. Wang, S. Zhang, H. Liu, S. Li, X. Wang, *J. Environ. Sci.* **2019**, *75*, 40.
- [10] J. You, Y. Guo, R. Guo, X. Liu, *Chem. Eng. J.* **2019**, *373*, 624.
- [11] S. P. Álvarez, M. A. M. Tapia, M. E. G. Vega, E. F. H. Ardisana, J. A. C. Medina, G. L. F. Zamora, D. V. Bustamante, in *Plant Nanobionics*, (Ed: R. Prasad), Springer, Cham **2019**, p. 333–370, [https://doi.org/10.1007/978-3-030-12496-0\\_12](https://doi.org/10.1007/978-3-030-12496-0_12).
- [12] A. Truppi, F. Petronella, T. Placido, M. Striccoli, A. Agostiano, M. Curri, R. Comparelli, *Catalysts* **2017**, *7*, 1.
- [13] M. R. D. Khaki, M. S. Shafeeyan, A. A. A. Raman, W. M. A. W. Daud, *J. Environ. Manage.* **2017**, *198*, 78.
- [14] R. Fagan, D. E. McCormack, D. D. Dionysiou, S. C. Pillai, *Mater. Sci. Semicond. Process.* **2016**, *42*, 2.
- [15] P. Kodithuwakku, D. R. Jayasundara, I. Munaweera, R. Jayasinghe, T. Thoradeniya, M. Weerasekera, P. M. Ajayan, N. Kottegodda, *Prog. Solid State Chem.* **2022**, *67*, 100369.
- [16] N. Castro-Alarcón, J. L. Herrera-Arizmendi, L. A. Marroquín-Carteño, I. P. Guzmán-Guzmán, A. Pérez-Centeno, M. Á. Santana-Aranda, *Microbiol. Res. J. Int.* **2016**, *4*, 55.
- [17] S. M. H. AL-Jawad, A. A. Taha, M. M. Salim, *Optik* **2017**, *142*, 42.
- [18] M. Nasirian, C. F. Bustillo-Lecompte, M. Mehrvar, *J. Environ. Manage.* **2017**, *196*, 487.
- [19] D. Wang, S. C. Pillai, S.-H. Ho, J. Zeng, Y. Li, D. D. Dionysiou, *Appl. Catal., B* **2018**, *237*, 721.
- [20] P. Bhattacharya, S. Neogi, *Rev. Chem. Eng.* **2019**, *35*, 861.

- [21] T. K. Jana, A. Pal, A. K. Mandal, S. Sarwar, P. Chakrabarti, K. Chatterjee, *ChemistrySelect* **2017**, *2*, 3068.
- [22] M. H. H. Mahmoud, A. A. Ismail, M. M. S. Sanad, *Chem. Eng. J.* **2012**, *187*, 96.
- [23] J. A. Torres-Luna, N. R. Sanabria, J. G. Carriazo, *Powder Technol.* **2016**, *302*, 254.
- [24] S. Zhao, D. Kang, Z. Yang, Y. Huang, *Appl. Surf. Sci.* **2019**, *488*, 522.
- [25] T. Charitha, U. Leshan, M. Shanitha, W. Ramanee, L. Buddi, B. Martin, *Results Mater.* **2021**, *12*, 100219.
- [26] L. Usgodaarachchi, C. Thambiliyagodage, R. Wijesekera, S. Vigneswaran, M. Kandanapitiye, *ACS Omega* **2022**, *7*, 27617.
- [27] N. Kumar, S. C. Dubey, P. Kumar, S. M. P. Khurana, *Indian Phytopathol.* **2019**, *72*, 367.
- [28] T. A. I. Lasheen, *Hydrometallurgy* **2005**, *76*, 123.
- [29] N. A. Jabit, G. Senanayake, *J. Phys.: Conf. Ser.* **2018**, *1082*, 012089.
- [30] A. R. Gharakhlou, M. N. Sarvi, *Mater. Res. Express* **2017**, *4*, 1.
- [31] Z. Li, Z. Wang, G. Li, *Powder Technol.* **2016**, *287*, 256.
- [32] D. Wibowo, M. Nurdin, M. Maulidiyah, A. H. Watoni, N. Jabit, *Int. J. ChemTech Res.* **2016**, *9*, 483.
- [33] Y. R. Smith, K. Joseph Antony Raj, V. (Ravi) Subramanian, B. Viswanathan, *Colloids Surf., A* **2010**, *367*, 140.
- [34] T. Murashige, F. Skoog, *Physiol. Plant.* **1962**, *15*, 473.
- [35] I. Mosa, M. Ehwaeti, E. Akkuzu, *Kastamonu Univ. J. For. Fac.* **2017**, *17*, 362.
- [36] H. L. Barnett, B. H. Barry, *Illustrated Genera of Imperfect Fungi*, 4th ed., APS Press, St. Paul, MN **2010**.
- [37] W. A. P. J. Premaratne, N. A. Rowson, *Phys. Sep. Sci. Eng.* **2003**, *12*, 13.
- [38] S. Gupta, M. Tripathi, *Open Chem.* **2012**, *10*, 279.
- [39] K. L. Seneviratne, I. Munaweera, S. E. Peiris, C. N. Peiris, N. Kottegoda, *Iran. J. Catal.* **2021**, *11*, 217.
- [40] T. P. B. Rajakaruna, C. P. Udawatte, R. Chandrajith, R. M. G. Rajapakse, *ACS Omega* **2020**, *5*, 16176.
- [41] H. H. Ahn, M. S. Lee, *Miner. Process. Extr. Metall. Rev.* **2020**, *42*, 312.
- [42] M. Nurdin, A. Zaeni, M. Maulidiyah, M. Natsir, A. Bampe, D. Wibowo, *Orient. J. Chem.* **2016**, *32*, 2713.
- [43] M. H. H. Mahmoud, A. A. I. Affi, I. A. Ibrahim, *Hydrometallurgy* **2004**, *73*, 99.
- [44] P. S. Parapari, M. Irannajad, A. Mehdilo, *Miner. Eng.* **2016**, *92*, 160.
- [45] A. A. Baba, F. A. Adekola, E. E. Toye, R. B. Bale, *J. Miner. Mater. Charact. Eng.* **2009**, *08*, 787.
- [46] N. El-Hazek, T. A. Lasheen, R. El-Sheikh, S. A. Zaki, *Hydrometallurgy* **2007**, *87*, 45.
- [47] T. Tao, Y. Chen, D. Zhou, H. Zhang, S. Liu, R. Amal, N. Sharma, A. M. Glushenkov, *Chemistry* **2013**, *19*, 1091.
- [48] X. Lin, Z. Qu, Y. Chen, R. Jin, T. Su, Y. Yu, S. Zhu, M. Huo, J. Peng, Z. Wang, *Sci. Rep.* **2019**, *9*, 1.
- [49] E. Albitter, M. A. Valenzuela, S. Alfaro, G. Valverde-Aguilar, F. M. Martínez-Pallares, *J. Saudi Chem. Soc.* **2015**, *19*, 563.
- [50] A. Zielińska, E. Kowalska, J. W. Sobczak, I. Łącka, M. Gazda, B. Ohtani, J. Hupka, A. Zaleska, *Sep. Purif. Technol.* **2010**, *72*, 309.
- [51] J. C. Durán-Álvarez, V. A. Hernández-Morales, M. Rodríguez-Varela, D. Guerrero-Araque, D. Ramirez-Ortega, F. Castillón, P. Acevedo-Peña, R. Zanella, *Catal. Today* **2020**, *341*, 71.
- [52] C. Powell, X-Ray Photoelectron Spectroscopy Database XPS, Version 4.1, NIST Standard Reference Database 20, **1989**. <https://doi.org/10.18434/T4T88K>.
- [53] B. Xin, L. Jing, Z. Ren, B. Wang, H. Fu, *J. Phys. Chem. B* **2005**, *109*, 2805.
- [54] P. Dong, F. Yang, X. Cheng, Z. Huang, X. Nie, Y. Xiao, X. Zhang, *Mater. Sci. Eng., C* **2019**, *96*, 197.
- [55] L. Gao, W. Gan, S. Xiao, X. Zhan, J. Li, *RSC Adv.* **2015**, *5*, 52985.
- [56] La Russa, M. F., A. Macchia, S. A. Ruffolo, F. De Leo, M. Barberio, P. Barone, G. M. Crisci, C. Urzi, *Int. Biodeterior. Biodegrad.* **2014**, *96*, 87.
- [57] S. Saroj, L. Singh, R. Ranjan, S. V. Singh, *Res. Chem. Intermed.* **2019**, *45*, 1883.
- [58] C. V. Tran, P. T. H. Nguyen, D. A. Nguyen, B. T. Le, T. N. Truong, D. D. La, *Int. J. Adv. Eng. Manage. Sci.* **2018**, *4*, 574.
- [59] L. D'Souza, P. Devi, D. Shridhar, C. G. Naik, *Anal. Chem. Insights* **2008**, *3*, 135.
- [60] M. R. A. Kumar, B. Abebe, P. Nagaswarupa, C. A. Murthy, C. R. Ravikumar, F. K. Sabir, *Sci. Rep.* **2020**, *10*, 1249.
- [61] ICP-OES and ICP-MS Detection Limit Guidance, <https://www.eag.com/resources/appnotes/icp-oes-and-icp-ms-detection-limit-guidance/2015-2022>.
- [62] R. Nair, S. H. Varghese, B. G. Nair, T. Maekawa, Y. Yoshida, D. S. Kumar, *Plant Sci.* **2010**, *179*, 154.
- [63] J.-S. Min, K.-S. Kim, S.-W. Kim, J.-H. Jung, K. Lamsal, S.-B. Kim, M.-Y. Jung, Y.-S. Lee, *Plant Pathol. J.* **2009**, *25*, 376.
- [64] K. Safavi, F. Mortazaeinezhad, M. Esfahanizadeh, H. Dastjerd, in *Proc. of Int. Conf. on Life Science and Technology*, IPCBEE, Singapore **2011**, p 159–161.
- [65] M. K. Sarmast, H. Salehi, *Mol. Biotechnol.* **2016**, *58*, 441.
- [66] A. Khezerlou, M. Alizadeh-Sani, M. Azizi-Lalabadi, A. Ehsani, *Microb. Pathog.* **2018**, *123*, 505.
- [67] J. Kiwi, V. Nadochenko, *J. Phys. Chem. B* **2004**, *108*, 17675.